RESEARCH ARTICLE

Turbulence Characteristics of Wind-Speed Fluctuations in the Presence of Open Cells: A Case Study

Xiaoli G. Larsén[1] · **Søren E. Larsen[1]** · **Erik L. Petersen[1]** · **Torben K. Mikkelsen[1]**

Abstract

Open cellular structures are frequently observed accompanying cold fronts over the North Sea. Through a two-day case study, measurements from two sites that are 100 km apart, and both covered by open cells, show that the turbulence is characterized by (1) considerable energy in the spectral gap region; (2) similar large-scale wind variation from surface to 100 m. These observations challenge existing algorithms for calculating parameters relevant to wind energy, including the turbulence intensity. We suggest that, in the presence of open cells, the stability effect is more related to the large-scale process, while the conventional parameter, the surface-layer Obukhov length, is less suitable. This issue is also revealed by the comparison of measurements with an unstable-boundary-layer spectral model. A mesoscale spectral model $Aa_1 f^{-2/3}$ is proposed to include the stability effect, when combined with a boundary-layer turbulence model for neutral conditions. The stability effect is introduced to this mesoscale model in a simple manner through calibration, with the coefficient A obtained from regression using standard 10-min time series (from measurements or numerical modelling). The combined model successfully reproduces the power spectrum of wind-speed fluctuations for the two-day open-cell event.

Keywords Turbulence models · Mesoscale spectral model · Open cells

1 Introduction

1.1 Spectral Behaviour of Wind Speed

Many classical boundary-layer turbulence theories rely on the condition of the existence of a gap in the wind-speed spectrum, since the basic assumptions of ergodicity and stationarity require such a gap. In the development of spectral forms for the energy-containing range, it has been assumed that this gap exists, separating boundary-layer turbulence from external fluctuations (Kaimal et al. 1972). Decades of studies on the spectral gap were reviewed in Larsén et al. (2016), which validated a spectral model for the gap region using two years

✉ Xiaoli G. Larsén
  xgal@dtu.dk

[1] Wind Energy Department, Risø Campus of the Danish Technical University, Frederiksborgvej 399, 4000 Roskilde, Denmark

of 20-Hz sonic anemometer measurements from a coastal site in Denmark. Their model suggests that, climatologically, the three-dimensional (3D) boundary-layer turbulence and the large-scale two-dimensional (2D) fluctuations are at most weakly correlated in the gap region, and the spectral energy in the gap region is a simple superposition of the 2D and 3D spectral power. This gap-region spectral model is applied and adjusted here in the presence of open cells. Hereafter we use the word "turbulence" to characterize atmospheric stochastic processes, including the local 3D and large-scale 2D processes.

Existing 3D turbulence studies focus on stationary homogeneous flow in the boundary layer (e.g. Kaimal et al. 1972, 1976; Mann 1994). Stationarity implies the existence of a single outer integral time scale Λ_s, at which the spectral power $S(f)$ levels off towards lower frequencies. Such stationarity is presented as a f^{+1} slope for the lower frequencies when $fS(f)$ is plotted versus f in log-log coordinates, according to the Wiener-Khintchine theorem for a stationary and random process; here f is the frequency. This spectral behaviour of a f^{+1} slope has often been confirmed in the analysis of 10–30 min measurement time series. Conventionally, at a height of 10 m, a data length of 10 min is usually applied, but at greater heights, eddies are of larger scales, which causes the peak of the spectrum to move systematically towards lower frequencies, requiring longer time series. Similarly, the same requirement for longer time series should also apply for unstable stratification where larger scale eddies are involved. The choice of a time series with a length not longer than e.g. 30 min is favourable for excluding the extra fluctuations at mesoscale frequencies. In attempts to remove the non-stationarity in the time series, a detrending process, sometimes in connection with the use of a Hanning window, is often applied to the time series before calculating the spectrum.

These numerical manipulations of data do not, however, remove the active turbulence. Studies have reported the absence of the spectral gap in the presence of features such as longitudinal vortices, rolls, jets, and convective cells (LeMone 1976; Smedman 1991; Smedman et al. 1995; Heggem et al. 1998; Larsén et al. 2016). Etling and Brown (1993) provided a review of unstable and coherent structures such as vortices, large eddies, and rolls in the planetary boundary layer, with a particular focus on roll vortices, covering measurement, theory and numerical modelling. It summarized the fact that different organized convective structures form during different unstable conditions. In the presence of rolls, flight data showed distinct peaks in the velocity and temperature spectra at scales matching the rolls, resulting in deviations of the spectra from conditions in the absence of the organized structures. Brummer et al. (1992) observed that, in the presence of boundary-layer rolls over the Atlantic Ocean, there is significant extra spectral energy in a number of meteorological variables in the range of 0.015 to 0.05 Hz, with a spectral peak at about 0.025 Hz. Smedman (1991) observed the extra spectral energy related to boundary-layer rolls over the Baltic Sea from an even lower frequency range, 10^{-4} to about 10^{-2} Hz, with a spectral peak at about 2×10^{-3} Hz. Larsén et al. (2013, 2016) observed, with measurements from Horns Rev that, in the presence of the open cells (see Sect. 1.2), extra spectral energy is significant in the range from about 5×10^{-5} to about 10^{-2} Hz. The extra energy observed in these studies extends over a wide and varying frequency, or corresponding wavenumber (k), range, which frequently includes the typical boundary-layer 3D turbulence f or k domain. The source of the extra energy is related to the large-scale flow, in contrast to typical 3D turbulence, which is locally generated from the surface.

1.2 Open Cells

Over the North Sea, boundary-layer rolls, jets, and open cells are frequently observed in connection with storms. The current study focuses on the turbulence characteristics of wind-speed fluctuations in the presence of open-cell structures, since they affect a series of calculations important for wind-energy applications, especially for the large offshore wind farms.

Open cells frequently occur within cold-air outbreaks (Atkinson and Zhang 1996), where cold air is modified by the warm water, leading to the formation of clouds, often in the form of cloud streets roughly oriented along the mean wind direction. Further downwind in the outbreak, the cloud street transforms into open-cell structures (Brummer et al. 1992). Figure 1 shows a cloud photograph of the open-cell case studied here, where one can see the circular nature of clouds, which is associated with upwards motion and, in the centre, clear sky associated with downwards motion. As a result, there are both large spatial and temporal fluctuations in the wind speed and direction. Larsén et al. (2017b) showed that, in the presence of open cells, the 10-m wind speed can vary by as much as 5 m s^{-1} within 3 km, through the analysis of a synthetic aperture radar wind field during storm Britta.

Busack et al. (1985) found that the area around Weathership M in the north-eastern Atlantic is covered with open cells approximately 20% of the time. Open-cell structures can often be seen from satellite images over the Atlantic Ocean following the passage of cold fronts. Bakan and Schwarz (1992) surveyed four years (1980–1983) of NOAA satellite images for the north-east Atlantic for presence of convective clouds, and found that only 111 days in the four years did not display these convective phenomena over the ocean. The monthly frequency of open cells for the 4-year period was 60–90% in winter, and about 10–30% in summer. The majority of open-cell cases was observed between 55°N and 75°N. Bakan and Schwarz (1992) also reported that the average diameter of the collected open-cell cases was 41 km with a standard deviation of 15 km, although the size is dependent on the latitude: cases with diameters of 20–30 km prevailed north of 70°N, while diameters of 50–60 km were most abundant south of 60°N. In the Project "Extreme winds and waves for offshore turbines" (Larsén et al. 2017a), 429 storm days from 1994–2016, and mostly occurring during late autumn and winter, were simulated using the Weather Research and Forecasting (WRF) model at a spatial resolution of 2 km. An examination of the model wind fields showed that open cellular structure was present in 45% of the 429 days over the waters around Denmark.

The large-scale fluctuations in the wind field affect a number of applications related to wind energy such as turbine design and wind-farm control. In relation to wind-farm operation, Vincent (2010) explored the wind-speed fluctuations for scales of an hour or more and concluded that open cellular convection is a significant contributor to the mesoscale variability in wind speed at the Horns Rev wind farm.

The focus of the current study is to extend and combine earlier mesoscale studies of open-cell structures with higher frequency, 3D, turbulence analysis. The paper, through a case study, raises issues in describing turbulence in the presence of large-scale organized atmospheric structures. We benefit from the available sonic-anemometer measurements at two stations, Høvsøre and Horns Rev II mast 8 (hereinafter site M8, see Fig. 2), and analyze them together with results from three selected boundary-layer turbulence models. We examine the impact of open cellular structures on the vertical structure of turbulence of the wind field, and on the calculations of a key wind-energy parameters, the standard deviation of the turbulence of the longitudinal wind component, which is used to calculate the longitudinal turbulence intensity.

The measurements from the two sites used for turbulence analysis are introduced in Sect. 2, followed by the method for data analysis in Sect. 3. Section 4 shows the
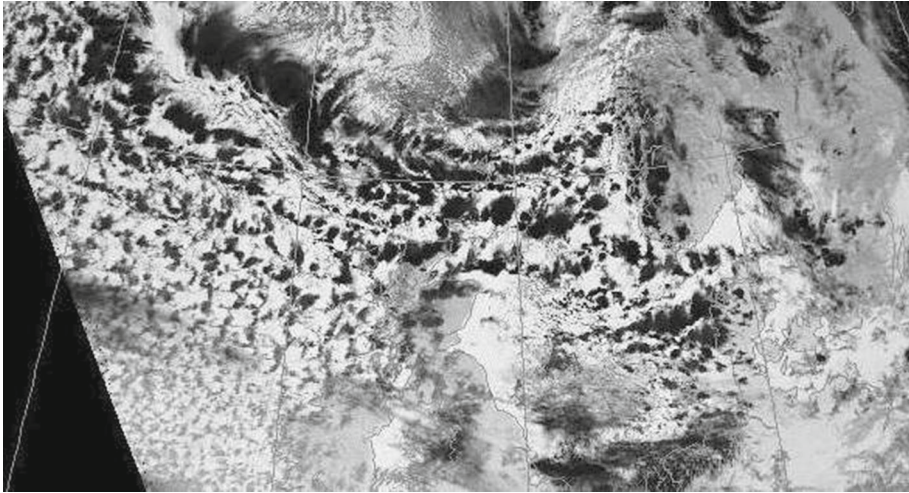
Fig. 1 Open cell clouds over the North Sea, Modis, ch22 received from satellite Terra on 3 December 2011 2133:05 (21 o′clock, 33 m and 5 s). The picture was downloaded from http://www.sat.dundee.ac.uk/abin/piccyjpeghtml/modis/2011/12/3/2133+42/ch22.jpg

analysis and results of the turbulence characteristics in the presence of open cells and the impact on the calculation of wind-speed variance. Discussions of methods, results and their implications for wind-energy applications are in Sect. 5. Conclusions are given briefly in Sect. 6, while Table 1 lists key variables and their definitions.

2 Measurements

Measurements from two sites are used: the near coastal land-based site Høvsøre, which is about 1.7 km from the west coast of Denmark, and the offshore site M8. The two sites are about 100 km apart and their locations are shown in Fig. 2. The turbulence characteristics during an open cell event are examined through a case study. The case includes two days, 3 and 4 December 2011, which were chosen because various measurements were simultaneously available at both Høvsøre and site M8. The cloud photograph, Fig. 1, shows the open cells at 2133:05 on 3 December.

At Høvsøre, standard wind measurements of 10-min averages are available at 10, 20, 40, 60, 80, 100 and 116.5 m, and 20-Hz sonic data are available at 10, 20, 40, 60, 80 and 100 m. Only sonic measurements at 10, 20, 80 and 100 m were used since issues have been reported for data during selected measurement periods at 40 and 60 m (Larsén et al. 2016). The 10-min averages of temperature at 10 m and 100 m, and pressure at 2 m and 100 m are also available. Details of measurements at Høvsøre can be found in Peña et al. (2016).

At site M8, standard 10-min averaged wind data are available at 27, 37, 47, 67, 77, 87, 97 and 107 m, and 0.1-Hz sonic data are available at 107 m. The 10-min averages of temperature at 23 and 101 m, and the sea-surface temperature (SST) are also available. The sonic data were sampled at 5 Hz, but only stored disjunctively at a frequency of 0.1 Hz, thus only the frequency part of the 3D turbulence spectrum below the Nyquist frequency of 0.05 Hz was sampled. However, when used together with the 20-Hz sonic data from Høvsøre, this is sufficient for the purpose of examining the spectral properties related to the open cells.

Fig. 2 Map of Denmark and the location of Høvsøre and Horns Rev II site M8
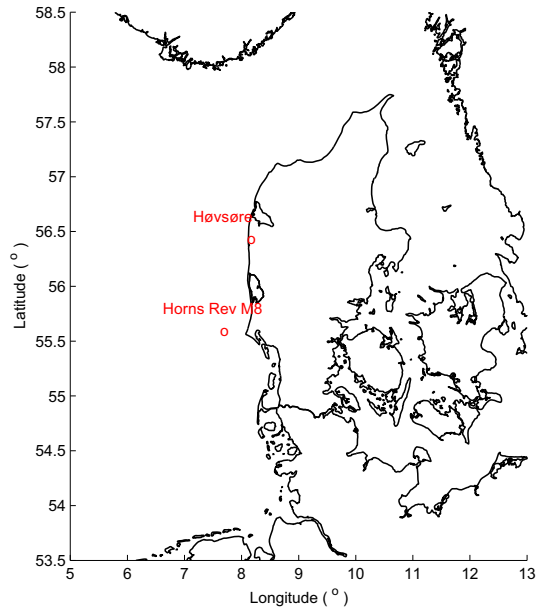
The 10-min mean data coverage is 100% for both sites. At site M8, the sonic data are missing from 6 am to 10 am on 3 December, and from 8 pm to midnight on 4 December. For the remaining 35 hours, sonic data are available, with 28 hours having 100% data coverage. At Høvsøre, the sonic data have 100% data coverage for both days.

3 Method

3.1 Stability Effect

To examine the effect of atmospheric stratification, we use the Richardson number Ri and the Monin–Obukhov stability parameters z/L, where L is the Obukhov length. At Høvsøre, we have the data required to calculate both z/L and Ri, where z/L is calculated at height $z = 10$ m, 20 m, 80 m and 100 m, and L is given by

$$L = -\frac{u_*^3 T_0}{\kappa g \overline{w'\theta_v'}}, \tag{1}$$

where T_0 is the mean temperature at height z, $u_* = (\overline{u'w'}^2 + \overline{v'w'}^2)^{0.25}$ is the friction velocity, g is the acceleration due to gravity, κ is the von Kármán constant 0.4, and $\overline{w'\theta_v'}$ is the virtual heat flux at z. The calculation of the turbulence fluxes was based on the standard 10-min-long time series. The Richardson number Ri was calculated using measurements from two heights, z_1 and z_2, using

$$Ri = \left(\frac{g}{\overline{\theta}}\right) \frac{\Delta\theta}{\Delta z} \Big/ \left(\frac{\Delta U}{\Delta z}\right)^2, \tag{2}$$

where $\Delta z = z_2 - z_1$, $\Delta\theta = \theta_{z_2} - \theta_{z_1}$, and $\overline{\theta} = (\theta_{z_1} + \theta_{z_2})/2$ is the averaged potential temperature between height z_1 and z_2, with $z_1 = 10$ m and $z_2 = 100$ m. Compared to z/L

Table 1 Variables and definitions

Variable	Definition
a	A coefficient related to the magnitude of spectral energy, as in Eq. 5
a_1	A coefficient in the spectral model for low frequencies, as in Eqs. 6 and 7
a_2	A coefficient in the spectral model for low frequencies, as in Eq. 6
A	A coefficient to adjust the mesoscale model to measured energy level
f	Frequency (Hz)
f_c	Coriolis parameter (Hz)
f_p	Peak frequency of the 3D turbulence spectrum (Hz)
g	Acceleration due to gravity (m s^{-2})
h	Neutral boundary-layer height (m)
k	Longitudinal wavenumber (m^{-1})
L	Obukhov length (m)
$L_{10}, L_{20}, L_{80}, L_{100}$	Obukhov length at 10 m, 20 m, 80 m and 100 m (m)
n	Normalized frequency (fz/U)
n_i	fz_i/U as in Eq. 4
n_l	z/Λ_s as in Eq. 5
n_{ru}	$n_{ru} = f_{ru}z/U$, as in Eq. 4
n_u	0.185 as in Eq. 5
Ri	Richardson number Eq. 2
Ri_B	Bulk Richardson number
S	Power spectrum of wind fluctuations, (m^{-2} s^{-1})
S_l	Large-scale wind spectral model, Eq. 6, (m^{-2} s^{-1})
S_u	Power spectrum of u-component of wind velocity (m^{-2} s^{-1})
T_0	Temperature (K)
U	Wind speed (m s^{-1})
u, v, w	The along-wind, cross-wind and vertical wind component (m s^{-1})
u_*	Friction velocity (m s^{-1})
z	Height (m)
z_i	Convective boundary-layer height (m)
z_1, z_2	The first and second height for calculating Ri (m)
$-\overline{u'w'}, -\overline{v'w'}$	Momentum fluxes (m^{-2} s^{-2})
$\overline{w'\theta'_v}$	Virtual heat flux (m s^{-1} K)
κ	von Kármán constant, 0.4
σ_U	Standard deviation of wind-speed fluctuations (m s^{-1})
Λ_s	The single outer length scale (m)

calculated from flux measurements at height z, Ri represents an average estimate of the stability between z_1 and z_2.

At site M8, we have only data with which to calculate Ri, since the sonic data are stored disjunctively at a low sampling frequency of 0.1 Hz, which is significantly lower than the spectral peak of w. This creates difficulty in calculating directly the momentum fluxes $\overline{u'w'}$ and $\overline{v'w'}$, and accordingly the parameter z/L. Due to the availability of the SST (θ_s), however,

the Richardson number was calculated between sea surface $z_1 = 0$ and $z_2 = 23$ m, i.e. the so-called bulk Richardson number Ri_B. Thus, $Ri_B = (\frac{g}{\theta})(\frac{\theta-\theta_s}{z})/(\frac{U}{z})^2$, with θ and U the potential temperature and wind speed at $z = z_2$ and $\bar{\theta}$ is the averaged potential temperature between the sea surface and z_2.

3.2 Calculation of Spectra From Measurements

The power spectra of three velocity components (the along-wind component u, the cross-wind component v and the vertical component w) and the wind speed ($U = \sqrt{\overline{u^2} + \overline{v^2}}$) have been calculated from the sonic-anemometer measurements at Høvsøre and site M8. The first half day of the two-day period are not included in calculating u and v due to a significant change in the wind direction during that time. To include the spectral gap region, we calculated the spectra of u and v from a single time series of 36 h. The entire two-day time series was used for calculating the spectra of wind-speed fluctuations, since it is direction independent. The spectrum was calculated using a simple Fourier transform, with a linear detrending applied to the time series and a prime factor decomposition of the time series so that the data length is a power of 2. The spectrum is smoothed afterwards by averaging the values of the spectral power in bins of $\log_{10} f$, with 25 bins used for each decade.

3.3 Turbulence Models

We look first into the high-frequency 3D turbulence structure by examining three spectral models of atmospheric surface-layer turbulence: the neutral surface-layer spectral form from Kaimal and Finnigan (1994), hereinafter the Kaimal model; the spectrum for convective conditions from Højstrup (1982), hereinafter the Højstrup model; The spectrum model proposed by Mikkelsen et al. (2017) applicable to neutral atmospheric conditions and strong shear flow, hereinafter the Mikkelsen model.

The Kaimal model is chosen because it is the most-used, simple model. The Højstrup model is chosen because it is one of the very few turbulence models that takes into account the stability effect in convective conditions. The Mikkelsen model is chosen because it can reproduce the often observed spectral plateau that is absent in the Kaimal model. The spectral forms of the three spectra are illustrated in Fig. 3 as dashed curves for the typical wind speed at a height of 10 m.

The Kaimal model in a two-sided representation reads,

$$f S_u(f) = \frac{51 u_*^2 n}{(1 + 33n)^{5/3}}, \tag{3}$$

where $n = fz/U$ is the normalized frequency, with f in Hz, wind speed $U = U(z)$ where z is the measurement height above the ground in the surface layer, and the relationship between the friction velocity and roughness length z_0 is $\kappa U/u_* = \ln(z/z_0)$ in neutral conditions.

The Høstrup model introduces additional terms to the Kaimal model that account for thermally generated energy by applying mixed-layer scaling with the boundary-layer height z_i and the buoyancy flux (through the Obukhov Length at the surface, L). It reads,

$$f S_u(f) = \left(\frac{0.25 n_i u_*^2}{1 + 2.2 n_i^{5/3}} \right) \left(\frac{z_i}{-L} \right)^{2/3} + \frac{51 u_*^2 n_{ru}}{(1 + 33 n_{ru})^{5/3}} \beta, \tag{4}$$
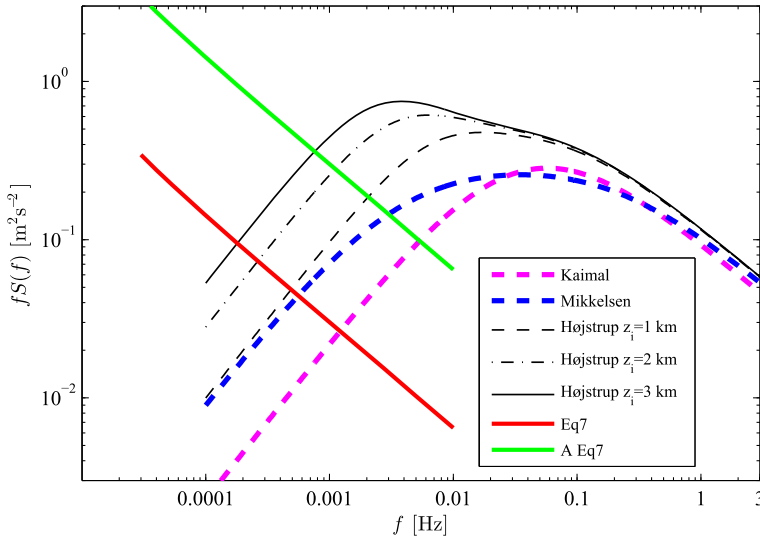
Fig. 3 Illustration of the three 3D turbulence models and the mesoscale model for the 10-m wind speed, with $A > 1$. For the Høstrup model, $z/L = -0.2$ is used, together with $z_i = 1$, 2 and 3 km, respectively

where $n_i = fz_i/U$, $n_{ru} = f_{ru}z/U$ with $f_{ru} = f/(1 + 15z/z_i)$ and $\beta = (1 - z/z_i)^2/(1 + 15z/z_i)^{2/3}$, where β increases with z_i but decreases with z. The difference between the Høstrup model and the Kaimal model can be seen in an example in Fig. 3 for $z = 10$ m, as a result of the stability term and β. The correction terms, f_{ru} and β, fine tune the behaviour of the peak frequency via z and the inertial subrange via z/L. One major challenge in using the Høstrup model is in determining the convective boundary-layer height z_i, which should be a function of stability and larger than the height of the neutral boundary layer $h = 0.2u_*/f_c$, where f_c is the Coriolis parameter. The overall value of h during the two days is calculated to be about 1.1 km. In the presence of the open cells, z_i is related to the height of open-cell cloud top, which is reported to be between 1 and 3 km (Atkinson and Zhang 1996). Thus we use $z_i = 1$ km, 2 km and 3 km to represent the near-neutral, average, and maximum cloud-top height for open cells.

The Mikkelsen model is a simple analytical model of boundary-layer turbulence that extends the Kaimal spectrum with a parametrization of a flat, near-surface shear production subrange ($fS(f)$ vs. f in log–log coordinates as shown in Fig. 3) (Tchen et al. 1985; Högström et al. 2002). Distinct shear-production subranges have been observed in several atmospheric turbulent spectra measured in the eddy surface layer, cf. e.g. Högström et al. (2002) and Mikkelsen et al. (2017). Thus, below the Kaimal model's classical peak frequency and nearest to the ground, the Mikkelsen spectrum predicts a shear-production subrange of f^0-power spectral law between the inertial subrange and the f^{+1}-power law at the lowest frequencies. As in both Kaimal and Høstrup models, the f^{+1}-power law is characteristic of a component spectrum with the single outer length scale Λ_s. The spectral model applies to the near-neutral atmospheric surface layer and the effect of the shear-production sublayer modifies the classical Kaimal spectrum at frequencies below the spectral peak at heights up to 50–60 m above the ground, cf. Mikkelsen et al. (2017). The Mikkelsen model reads,

$$fS_u(f) = \frac{0.5au_*^2 n/n_l}{(1 + n/n_l)(1 + n/n_u)^{2/3}} \tag{5}$$

where a is a coefficient related to the spectral energy level, n_l constrains f^{+1} at the low frequencies and it is related to the height of the neutral boundary layer, n_u discerns the transition between the shear-production subrange and the inertial subrange in the high-frequency region. Based on measurements needs from mid-latitudes, Högström et al. (2002) recommended $a = 0.953$, $n_u = 0.185$ and $n_l = z/\Lambda_s$ with $\Lambda_s = 3h$.

In the above three turbulence models, the Kaimal and the Mikkelsen models apply strictly to near-neutral atmospheric conditions. The Kaimal model provides more or less the same $fS(f)$ with height at the peak frequency f_p, with f_p shifting to lower frequencies with increasing height. The Mikkelsen and the Høstrup models, however, provide lower spectral energy at f_p for greater heights, and have f_p shifting to lower frequencies with increasing height. The Mikkelsen model, in the presence of strong shear, also estimates the often-observed plateau in the frequency range lower than f_p (see Fig. 3). For scales larger than n_l, the spectral energy levels off in all three models.

Similar to the combination of spectra with -3 and $-5/3$ slopes in the $k-$domain (Petersen 1975; Lilly and Petersen 1983; Gage and Nastrom 1985; Lindborg 1999), for $f << f_p$, Larsén et al. (2013) show that the point power spectrum in the $f-$domain, the large-scale variability wind-speed fluctuation spectrum, S_l, can be described similarly as,

$$S_l(f) = a_1 f^{-5/3} + a_2 f^{-3} \tag{6}$$

where $a_1 = 3 \times 10^{-4}$ m^2 s$^{-8/3}$ and $a_2 = 3 \times 10^{-11}$ m^2 s^{-4} are derived from offshore climatological wind datasets. This model is shown in Fig. 3 as the red solid curve. For $f > 1$ day^{-1}, $a_2 f^{-3}$ becomes much smaller than $a_1 f^{-5/3}$ and Eq. 6 can be simplified and reformed as

$$f S_l(f) = a_1 f^{-2/3}. \tag{7}$$

Following studies on the wavenumber spectrum in the literature, e.g. Gage and Nastrom (1985, 1986) and Lindborg (1999), Larsén et al. (2013) argued that $a_2 f^{-3}$ is related to planetary baroclinic instability and it is most effective for $f < 1$ day^{-1}. It was also shown that $a_1 f^{-5/3}$ is dominating for $1 < f < 72$ day^{-1}, the mesoscale range. In Larsén et al. (2013) it was observed that the mesoscale spectra calculated from 24-h sampled time series showed little response to the daily-averaged stability parameter Ri at Horns Rev I (between 15 and 62 m) and Nysted (between 15 and 45 m). Larsén et al. (2016, 2018) found the coefficient a_1 to change with upwind surface conditions; for instance, at 10 m, a_1 was shown to be smaller over land than over water due to the rougher surface and hence larger momentum sink. Larsén et al. (2016) observed that for special individual cases, such as storms in the presence of open cells, for $f > 1$ day^{-1}, $S_l(f)$ was significantly larger than values in Eq. 6 with a_1 and a_2 obtained from climatological measurements (their Fig. 12). This extra energy is illustrated by the green curve in Fig. 3 in contrast to the mesoscale spectral model (red curve).

This suggests that for our open-cell case, the use of the climatological mesoscale model from Larsén et al. (2013) needs to be recalibrated. In Fig. 4, the blue curve is the spectrum calculated from 20-Hz wind speeds at 10 m during our study case 3 and 4 December 2011, the red solid curve is Eq. 7, and the green solid curve is 10 times Eq. 7. For $f > 10^{-4}$ Hz, the spectral energy calculated from the measurement is significantly larger than that of the climatological condition (green curve vs. red curve). As will be shown later in Sect. 4, the mean wind speed during this period is about 16 m s^{-1}, the corresponding size to the frequency 10^{-4} Hz is about 40 km, in agreement with the reported open-cell size range of 41 ± 15 km (Bakan and Schwarz 1992). This supports the claim that the observed extra energy around the gap region, 10^{-4} Hz $< f < f_p$, is related to the open cells. We construct a hybrid 3D spectrum
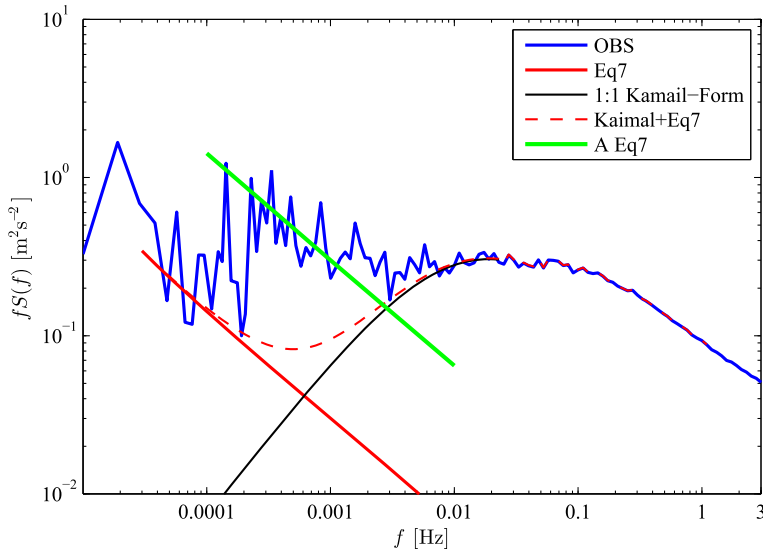
Fig. 4 Power spectrum of wind speed at 10 m at Høvsøre during 3 and 4 December 2011 from measurements. Also shown are Eq. 7 and Eq. 7 multiplied by coefficient A, with $A = 10$, the 1:1 Kaimal model form used for $f < f_p$ with $f_p = 0.02$ Hz and the red dashed curve is the sum of the red solid curve plus the black thin curve

using the shape of a Kaimal model with $f_p = 0.02$ Hz for $f < f_p$ and the measured spectrum for $f > f_p$. The sum of Eq. 7 and this hybrid 3D spectrum gives the red dashed curve in Fig. 4. Note that there is no 3D turbulence modelling involved in constructing the red-dashed curve. In Larsén et al. (2016), the hybrid spectrum matches the wind variation well over both 3D and 2D turbulence regimes (see their Fig. 8). For our open-cell case, the expected spectral gap is absent in the measurements at scales of 10 min to 1 h, where it contains extra energy, as approximated by the green curve.

Patching spectra from different frequency ranges began with Van der Hoven (1957), which included 3D turbulence measurements from one individual hurricane case, followed by Vinnichenko (1970) through an individual case for $z > 3$ km. Courtney and Troen (1990) first used data for a whole year at one height to show the full range of the wind-fluctuation spectrum. A concept for how spectra at different ranges can be put together was provided in a more general sense in Högström et al. (2002) and Kim and Adrian (1999), where they illustrated the possibility of using a simple superposition of the large-scale and boundary-layer turbulence. The quantification of such an idea was realized in Larsén et al. (2016), who used a mesoscale spectral model in the frequency domain, as derived from their earlier work (Larsén et al. 2013), together with microscale turbulence model concept. They demonstrated, using two years of measurements from Høvsøre and five years from Horns Rev I, that such a theory is valid, supporting the hypothesis that the mesoscale variability and 3D turbulence are at most only weakly correlated.

We reformulate the spectral model in Larsén et al. (2013) into $A a_1 f^{-2/3}$ for $f > 1$ day^{-1}, to describe the 2D wind variability. The coefficient A can be obtained through regression from the wind-fluctuation spectrum of the mesoscale range (see the green curve in Fig. 4 as an example). In the absence of the 10-min measurements, Larsén et al. (2017b) show that a mesoscale model such as the Weather Research and Forecasting (WRF) model can provide a reasonably good estimate of the wind-speed time series for a resolution of 10

min (see their Fig.9a), which in turn can be used to determine A. The coefficient A can thus include the overall mesoscale energy level for a particular case, where the case specific stability effect is included through the calibration process. This aspect of course means that the coefficient A is purely empirical and it has less claim to universality than many other coefficients within boundary-layer meteorology, which can be argued both on the basis of theories and measurements.

Adding $Aa_1 f^{-5/3}$ to the Kaimal model gives the fourth proposed model, referred to here as the Kaimal+Meso model

$$f S_u(f) = \frac{51 u_*^2 n}{(1 + 33n)^{5/3}} + Aa_1 f^{-2/3}. \tag{8}$$

Adding $Aa_1 f^{-5/3}$ to the Høstrup model gives a fifth model examined here, referred to as the Høstrup+Meso model

$$f S_u(f) = \left(\frac{0.25 n_i u_*^2}{1 + 2.2 n_i^{5/3}} \right) \left(\frac{z_i}{-L} \right)^{2/3} + \frac{51 u_*^2 n_{ru}}{(1 + 33 n_{ru})^{5/3}} \beta + Aa_1 f^{-2/3}. \tag{9}$$

And finally, adding $Aa_1 f^{-5/3}$ to the Mikkelsen model gives the sixth model combination, referred to as the Mikkelsen+Meso model

$$f S_u(f) = \frac{0.5 a u_*^2 \frac{n}{n_l}}{(1 + \frac{n}{n_l})(1 + \frac{n}{n_u})^{2/3}} + Aa_1 f^{-2/3}. \tag{10}$$

4 Results

Accompanying a cold-air outbreak observed on the first half day of 3 December 2011 at Høvsøre and site M8, the pressure decreased by 20 hPa and 15 hPa, respectively, see Figs. 5c and 6c. At the same time, the wind direction at the two sites changed by 80° from the south-west to the west-north-west. From noon on 3 December, at both sites, the winds were strong and the 10-min wind speed and direction fluctuated significantly; the change in the mean wind speed, from one 10-min period to another, was about 7 m s^{-1} at all levels, with the direction change about tens of degrees, see Figs. 5 and 6. The cloud photograph in Fig. 1 shows that open-cell structure covers both Høvsøre and site M8.

At site M8, the sea surface was 4–6 °C warmer than the atmosphere. The stability parameter Ri_B at site M8 between $z_1 = 0$ and $z_2 = 23$ m suggests unstable conditions (Fig. 6). At Høvsøre, stability is harder to interpret, since the mast is on land, 1.7 km from the coast. With flow from the sea, an internal boundary layer (IBL) will develop, leading to changing conditions with height. At lower levels, the land-surface conditions dominate, while higher up, the effect of the larger scale flow from the sea is found. This may explain the distinctive behaviour of z/L at 10 and 20 m compared to that at 80 and 100 m. At 10 m and 20 m, z/L values are in general positive, though very close to zero, with an average value of $L \approx 600$ m at 10 m and $L \approx 800$ m at 20 m (Fig. 5). While at 80 m and 100 m, z/L is mostly negative, with an average value of $L \approx -600$ m at 80 m and $L \approx -500$ m at 100 m, respectively. This follows the expected behaviour for a sea-influenced IBL. The values of z/L at 80 m and 100 m at Høvsøre suggest convective conditions, which is consistent with Ri_B at site M8. At Høvsøre, looking at the variation of Ri between 10 and 100 m together with z/L at several heights, one may deduce that the calculation of Ri at Høvsøre blends the local, slightly stable condition, and the large-scale, unstable condition.
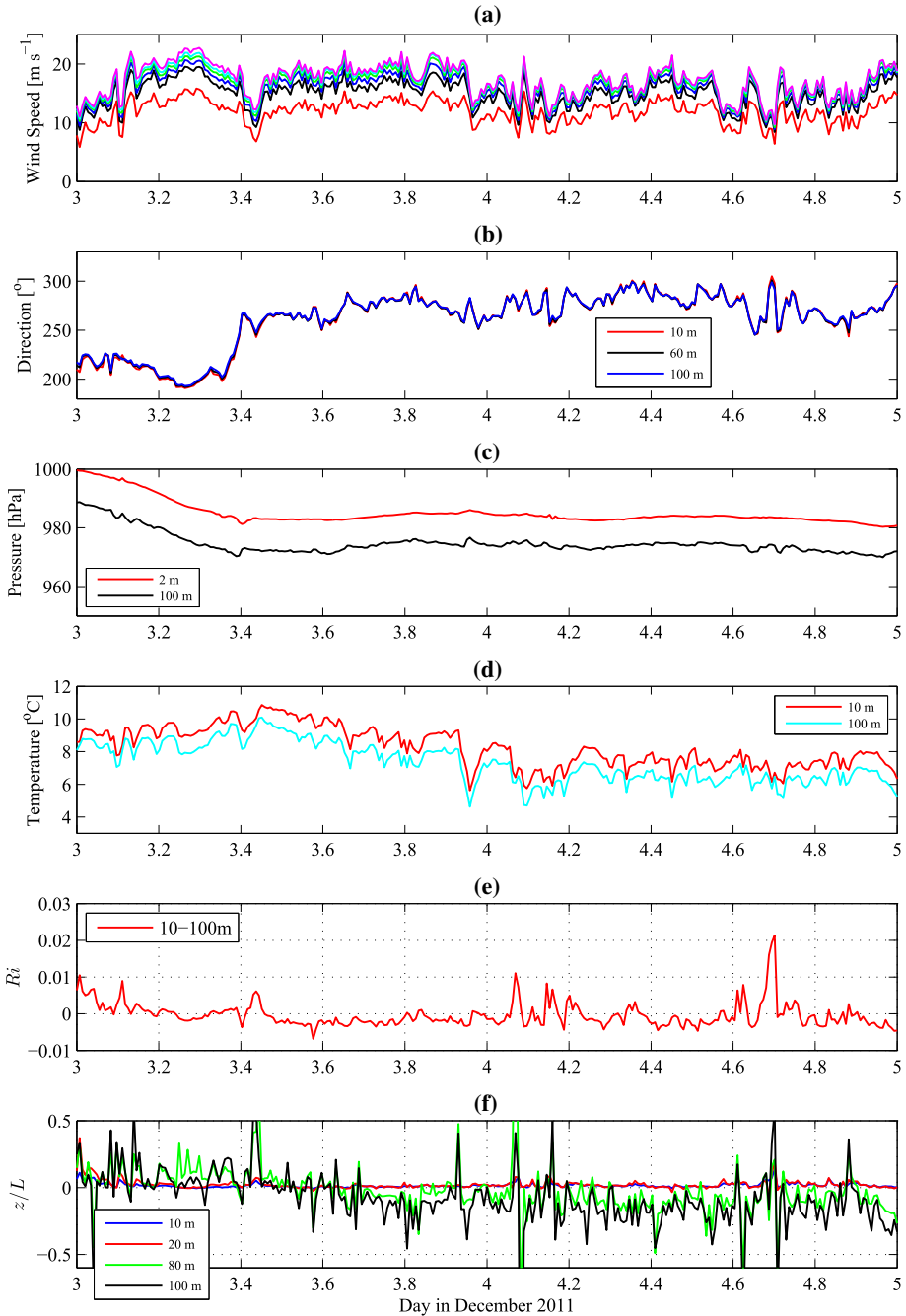
Fig. 5 The 10-min mean time series at several measurement heights at Høvsøre on 3 and 4 December 2011: **a** wind speed at 10, 40, 60, 80, 100 and 116.5 m (from below to up); **b** wind direction; **c** air pressure; **d** air temperature; **e** Richardson number; **f** z/L
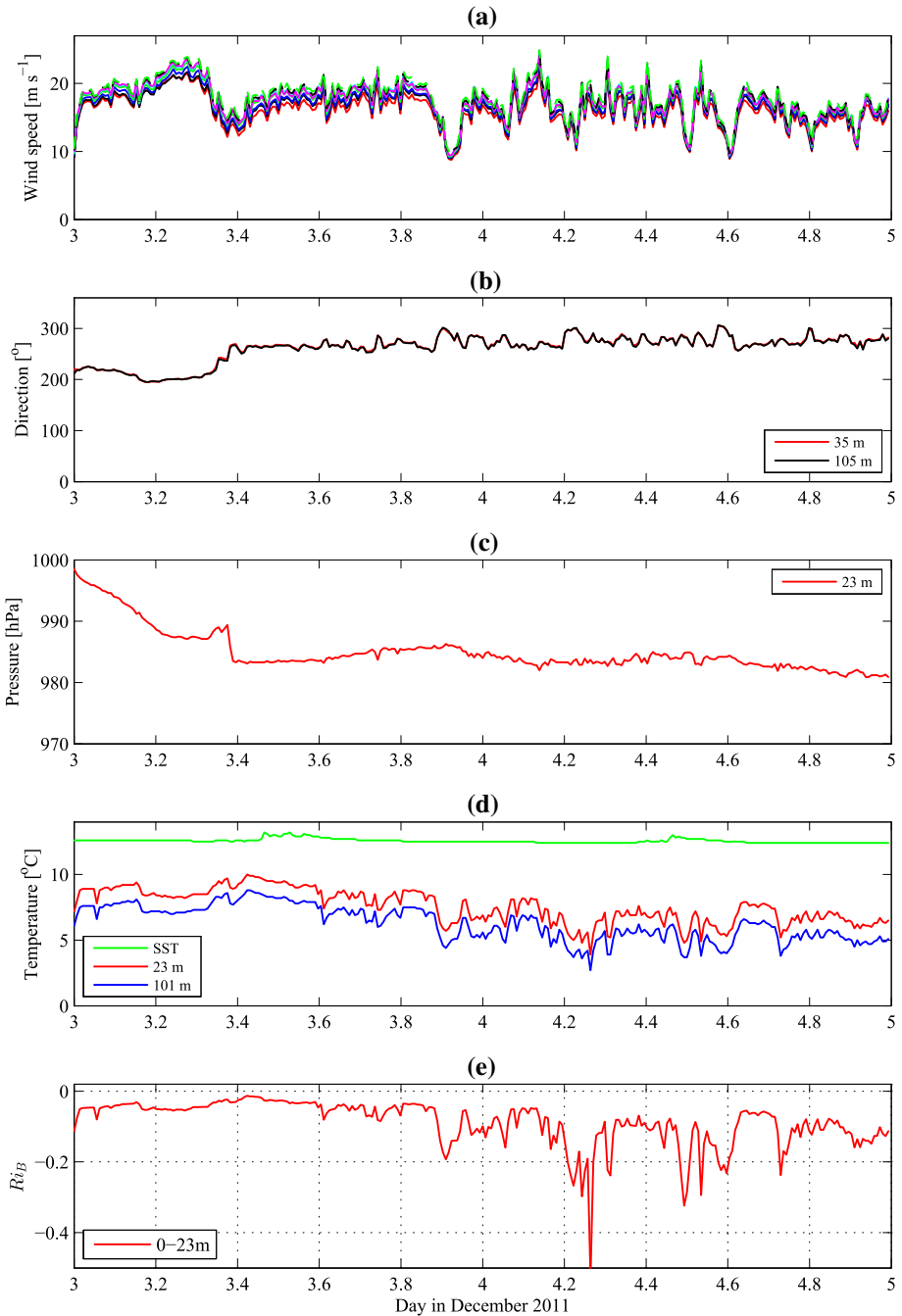
Fig. 6 10-min mean time series at several measurement heights at site M8 on 3 and 4 December 2011: **a** wind speed at 27, 37, 47, 67, 77, 87, 97 and 107 m (from below to up); **b** wind direction; **c** air pressure; **d** air and sea surface temperature; **e** bulk Richardson number

In the following, we first examine the turbulence structures in the presence of open cells from the Høvsøre site (Sect. 4.1); then we compare turbulence structures between Høvsøre and site M8 (Sect. 4.2); finally, we examine how the calculation of the standard deviation of wind-speed fluctuations, often used as a turbulence parameter, is affected by open-cell related turbulence (Sect. 4.3).

### 4.1 Turbulence Characteristics at a Single Site Høvsøre

In their studies of 2D and 3D turbulence, Larsén et al. (2016) used the measured 3D turbulence spectrum directly. The use of the Kaimal model in their study merely borrows the shape of the model to describe the leveling-off of the 3D spectral energy where $f < f_p$ (the black curve in Fig. 4). This process is shown in Fig. 4 as the hybrid spectrum through the red, dashed curve.

The blue curve from Fig. 4, the power spectrum of the 10-m wind-speed fluctuations at Høvsøre, is shown here in Fig. 7, together with the turbulence models. The Høstrup model Eq. 4 applies to $L < 0$, and since L at 10 m was positive at Høvsøre, only the Kaimal model and the Mikkelsen model are shown in Fig. 7a. Both models describe the inertial subrange well. Here we used a roughness length of $z_0 = 0.012$ m for Høvsøre, a reasonable value according to Peña et al. (2016) and Floors et al. (2016). Consistent with its description in Sect. 3.3, the Kaimal model has a rather narrow bandwidth (red dashed curve). The Mikkelsen model on the other hand has a broader spectrum (green solid curve, with $a = 1.1$ and $n_u = 0.185$ in Eq. 5).

In Fig. 7b, the large-scale wind fluctuation is included through Eqs. 8 (Kaimal+Meso) and 10 (Mikkelsen+Meso), which significantly improves the Kaimal and the Mikkelsen models for $f < f_p$. Due to the narrow spectral bandwidth with the Kaimal model, the energy is underestimated for 10^{-3} Hz $< f < f_p$, while Mikkelsen+Meso shows better agreement with the measurements. In using Eqs. 8 and 10, $A = 10$ was obtained from measurements using regression over $2 \times 10^{-4} < f < 10^{-3}$ Hz range.

Figure 8 shows similar plots as Fig. 7 but for 80 m. A roughness length of $z_0 = 0.004$ m was used, representing a upwind water surface condition, allowing all three 3D turbulence models to describe well the inertial subrange. The stability condition is unstable (Fig. 5f), allowing the use of the Høstrup model with $L_{80} = -600$ m. Three z_i values were tested, but only $z_i = 3$ km is shown. With $z_i = 1$ km, the Høstrup model is rather close to the Mikkelsen model, and with $z_i = 2$ km, the Høstrup model curve is located between the Mikkelsen and Kaimal models. With $z_i = 3$ km, which represents the highest open-cell cloud top, the Høstrup model is shown in Fig. 8 in dotted line. Adding the large-scale variation through $A a_1 f^{-5/3}$ to the Kaimal model actually gives a similar result as the Høstrup model for $f > 3 \times 10^{-3}$ Hz, cf. the black dotted curve and the red dashed curve in Fig. 8b. The uncertainty related to the use of z_i is rather high when using the Høstrup model. The Kaimal+Meso model slightly overestimates $f S(f)$ for $10^{-3} < f < 0.03$ Hz, while adding $A a_1 f^{-5/3}$ to the Mikkelsen model again gives a good fit to the measurements. At 80 m, A was found to be 12, suggesting an overall slightly higher mesoscale spectral energy at 80 m than at 10 m.

The power spectra from 10 m, 20 m, 80 m and 100 m from Høvsøre for the along-wind component u, cross-wind component v, and vertical wind component w are plotted in Fig. 9a, b, and c respectively. For high frequencies $f > 0.01$ Hz, we observe typical 3D turbulence behaviour: (1) the peak frequency for w is higher than that of v, which is itself higher than that of u; (2) for $f > f_p$, the spectral energy decreases with height, indicative of surface driven turbulence. For large scales with $f < 10^{-3}$ Hz, Fig. 9 suggests that the process is more
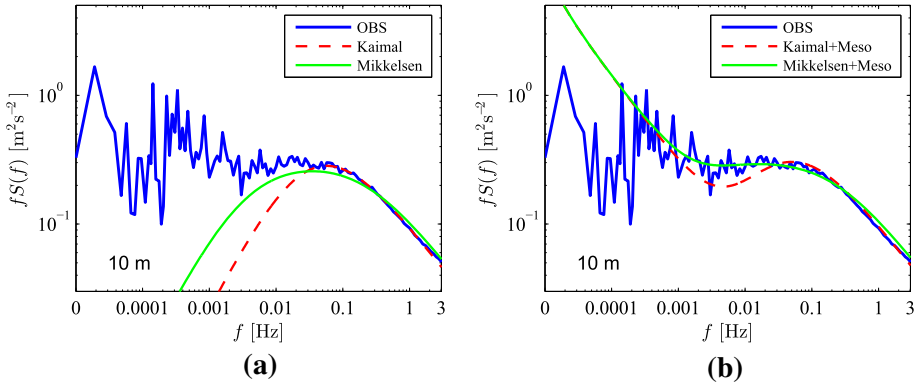
Fig. 7 a Power spectra of wind-speed fluctuations at 10 m at Høvsøre, calculated from the Kaimal and the Mikkelsen models and compared to measurements. **b** Power spectra of wind speed at 10 m from the Kaimal+Meso model and the Mikkelsen+Meso model, and compared to measurements
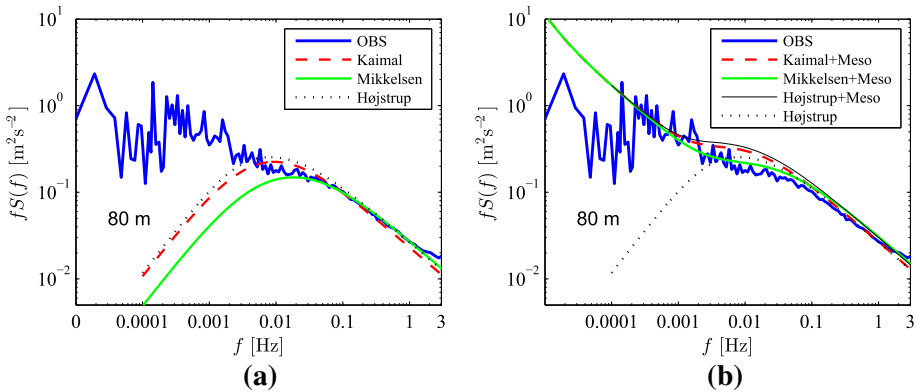
Fig. 8 a Power spectra of wind-speed fluctuations at 80 m at Høvsøre, calculated with measurements, from the Kaimal, the Høstrup and the Mikkelsen models. **b** Power spectra of wind speed at 80 m, from measurements, from the Kaimal+Meso model, the Høstrup+Meso model and the Mikkelsen+Meso model, as well as the Høstrup model. For the plot for the Høstrup model, $L_{80} = -600$ m and $z_i = 3$ km are used

top-down, shown as decreasing spectral energy of u, v, and w when approaching the surface, due to the net effect from the large-scale surface drag. However, for $f < 10^{-3}$ Hz, the energy and the fluctuation level are very similar for both u and v at all heights from the surface up to 100 m, suggesting a highly coherent 2D flow structure at all measurement levels.

4.2 Spectra of Wind Speed at Høvsøre and Site M8

As explained earlier, the data from site M8 do not include information for $f > 0.05$ Hz. For $f < 0.05$ Hz, the spectra are similar to those from Høvsøre, both in the shape and the level of energy. This is shown in Fig. 10a–c for the wind components u, v and w, respectively.

The similarity in the distribution of wind-speed fluctuations, as well as its energy level, throughout the frequency range from 1 day^{-1} to 0.2 Hz, is consistent with Fig. 1, which shows that both sites are covered by same pattern of open cells. Note that at the lowest
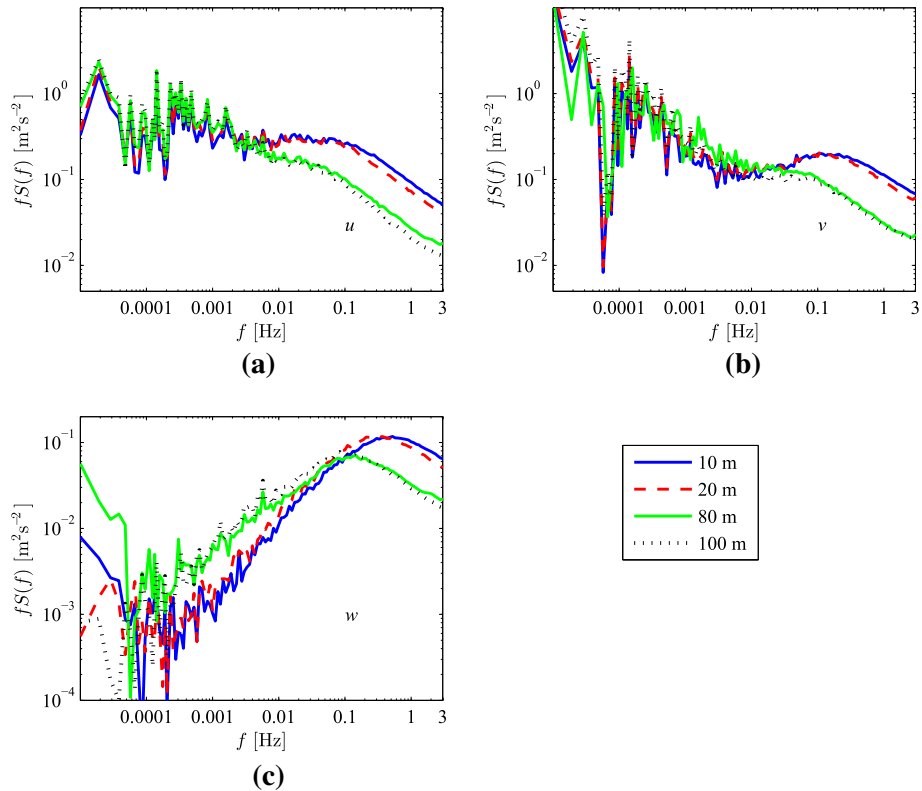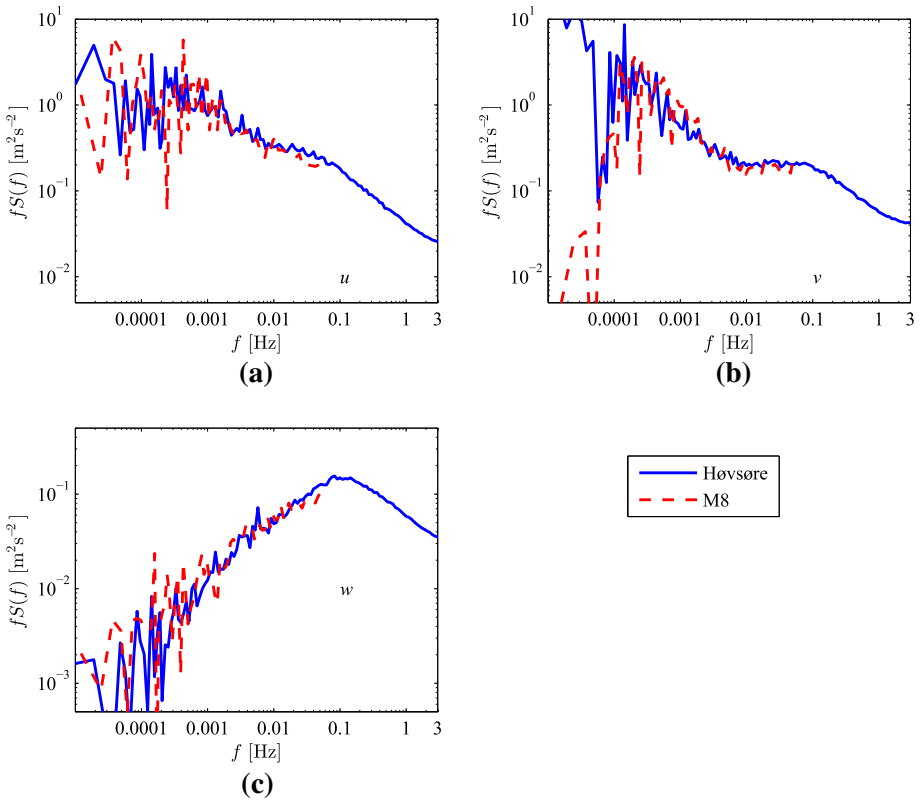
Fig. 9 Power spectra of, **a** along-wind velocity component u, **b** cross-wind velocity component v, and **c** vertical velocity component w at 10 m, 20 m, 80 m and 100 m at Høvsøre

frequencies, there are very few data points and the uncertainty is large, which likely explains the difference of the v-component for $f < 5 \times 10^{-5}$ Hz.

4.3 Calculation of the Standard Deviation of Wind Speed

As a standard procedure, classical turbulence models, such as the Kaimal model, are often used to calculate the variances and standard deviations of wind-speed fluctuations, σ_U, and wind components (u, v, and w), with a low-frequency limit of 10^{-3} Hz. These variables are important for the application of boundary-layer similarity theories and accordingly for wind-energy applications. However, the presence of an open cellular structure in the wind field challenges the use of these classical spectrum models and theories for calculating the appropriate turbulence parameters, which have limited ability to properly scale larger open-cell coherent structures observed at $f < f_P$.

We calculate σ_U using the 20-Hz wind speed time series over time periods varying from 10 min to 2 h during 3 and 4 December 2011 from Høvsøre. The estimates of these segments are averaged and the mean values are plotted as a function of the times series sampling time in Fig. 11, as black circles. The results are the same when a linear detrending is applied to the entire time series. The estimates using the Kaimal model and the Mikkelsen model

Fig. 10 Measured power spectra of, **a** along-wind velocity component u, **b** cross-wind velocity component v, **c** vertical velocity component w from Høvsøre (100 m) and site M8 (107 m) together

are shown as the red and green curve, respectively, using low-frequency limit ranging from 1.4×10^{-4} to 1.7×10^{-3} Hz, corresponding to time series that incrementally increases from 10 min to 2 hours. Figure 11a shows that, at 10 m, the Mikkelsen model gives a small underestimation of σ_U for the data length of 10 min, while the Kaimal model has a larger underestimation. Figure 11b shows that, at 80 m, using time series length of 10 min, the Kaimal model has a better estimate than the Mikkelsen model, but both again underestimate σ_U. As the length of the time series increases, meaning that lower frequency limit is used, both models predict leveled-off σ_U values due to the disappearance of energy for $f < 10^{-3}$ Hz, while the observed values of σ_U increase. With a time series length of 30 min, which is still commonly used, the deviation in the estimate of σ_U can be 20% or more. By adding the mesoscale wind variation, Kaimal+Meso and Mikkelsen+Meso, significantly improves the estimation. According to Fig. 11, Mikkelsen+Meso slightly outperforms Kaimal+Meso.

5 Discussion

As modern wind farms are increasing in size, with farm clusters reaching hundreds of km by hundreds of km, traditional boundary-layer turbulence models are limited in the ability to account for the flow variability over the entire farms. This is particularly the case for
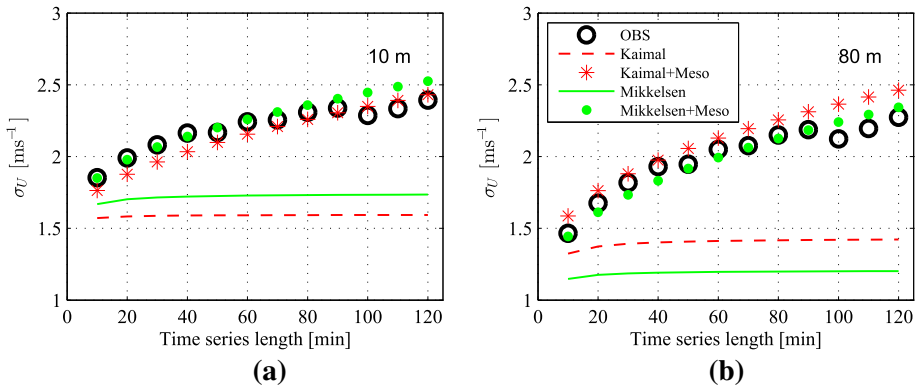
Fig. 11 The mean values of the estimate of σ_U at Høvsøre using wind speed during 3 and 4 December 2011 using time length of 10 min to 2 h **a** 10 m; **b** 80 m

offshore wind farms where organized atmospheric structures (such as open cells, gravity waves, and boundary-layer rolls) are common and persistent. Our study demonstrates the unusual turbulence structures and relevant issues related to the presence of open cells for wind-energy applications, through a case study.

Due to the availability of turbulence measurements at several heights at the coastal site, Høvsøre, we have been able to analyze the vertical turbulence characteristics over scales from the inertial subrange to the mesoscale range. The availability of the simultaneous turbulence measurement at an offshore site Horns Rev II mast 8 (site M8) made it possible to calculate and compare the wind and stability conditions across the large region affected by this event.

In the presence of open cells, the spectral analysis has revealed that there are two contributions to turbulence: the surface-driven turbulence at high frequencies and the large-scale turbulence at mesoscale frequencies. The surface-driven turbulence carries the classical characteristics. However, at mesoscale frequencies, the wind variation at Høvsøre is similar for all measurement heights from 10 to 100 m, suggesting a high coherence throughout the vertical region. The wind fluctuation is also shown to be similar at the two sites. This similarity is a challenge for existing algorithms for calculating the spatial distribution of wind-speed fluctuations that assume that winds are not correlated across such distances (Sørensen et al. 2002, 2008; Vincent et al. 2013; Mehrens et al. 2016). A quantitative description of the similarity of wind variation, e.g. through coherence analysis, could not be realized in this case study, since it requires considerable amounts of data.

To illustrate the challenges in modelling the 3D turbulence, three boundary-layer turbulence models are selected: two for neutral condition, (1) the most commonly used Kaimal model, and (2) the Mikkelsen model that is able to reproduce the frequenctly observed spectral plateau; and (3) the Høstrup model takes stability effect into account for convective conditions.

The two neutral models do not reproduce the significant amount of energy in the spectral gap region. This could be due to lack of stability effects, since many studies have observed greater energy within the gap region during convective conditions when compared with stable conditions, e.g. in Smedman-Högström and Högström (1974), Larsen et al. (1985), and Cheynet et al. (2018).

At high frequencies, the stability effect is related to n_u. The Kansas experiments have shown that the local stability affects the scaling of the inertial subrange (n_u), such that increasingly stable conditions correspond to higher n_u. However, in the range of $|z/L| < 0.2$,
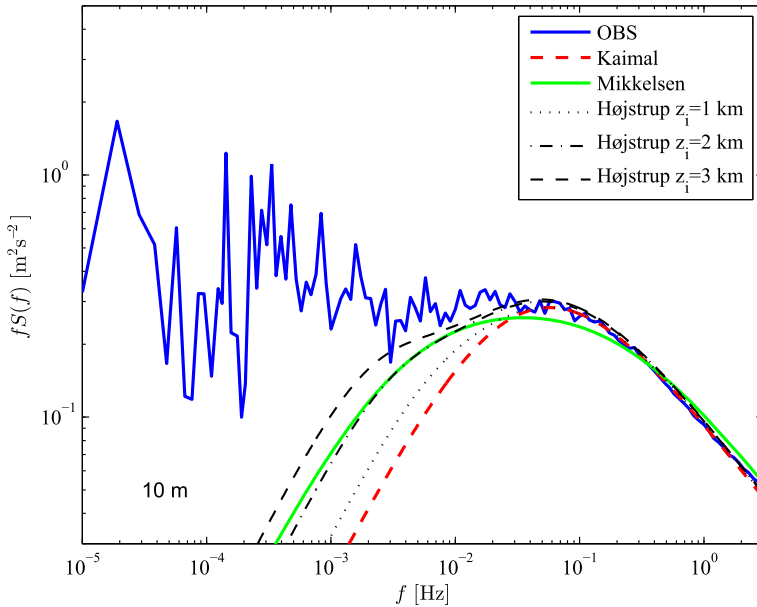
Fig. 12 Spectra of wind speed at 10 m, measurements at Høvsøre and Høstrup model using $L_{80} = -600$ m with $z_i = 1$, 2 and 3 km, together with the Kaimal and the Mikkelsen models as from Fig. 7a

n_u does not vary much (Kaimal et al. 1972). In our case, at Høvsøre, $|z/L|$ is generally less than 0.2, particularly close to the surface.

It was found that modelling the stability effect for this open-cell case is not easy. At Høvsøre, the Høstrup model underestimates the energy level for $f < f_p$ at 10 m, with the local stability $z/L_{10} \approx 0$. We relate the stability to the large-scale process following two calculations. First, the stability conditions at Høvsøre and site M8 are similar, as shown through the analysis using z/L_{100} from Høvsøre and Ri_B (0–23 m) from site M8. The relationships between z/L and Ri_B were derived in Businger et al. (1971) for different stability conditions, based on the data obtained during the summer of 1968 in western Kansas: $Ri_B = Cz/L$ for near-neutral ($C \approx 0.74$) and unstable conditions ($C \approx 1$), and Ri_B reaches the critical Richardson number at very stable condition. For site M8, if we use $Ri_B = z/L$ for unstable conditions and convert Ri_B to z/L, we obtain z/L comparable in magnitude to z/L at 80 and 100 m at Høvsøre. Second, encouraged by the coherent large-scale wind fluctuation from 10 to 100 m, using L from 80 m for the Høstrup model improves the turbulence modelling to 3×10^{-3} Hz $< f < f_p$ (see the black dotted curve in Fig. 12). Nevertheless, the improvement does not include the gap region between 10^{-4} and 10^{-3} Hz, where significant energy is still missing. Note that the Høstrup model describes an unstable surface layer underlying a simple well-mixed boundary layer, scaled by the convective boundary-layer height z_i and a convective velocity scale $w_* = (\frac{gz_i}{\theta}\overline{(w'\theta')}_s)^{1/3}$, where $\overline{(w'\theta')}_s$ is the surface heat flux. The model was calibrated initially with data from the Kansas 1968 and Minnesota 1974 experiments. In those data, no large-scale coherent structure was present and the spectral function tapers off with an f^{+1} low-frequency region. One reason may be the absence of significant mesoscale activity during the unstable Kansas and Minnesota experiments, being that they were mid-summer and mid-continental measurements over homogeneous flat land. Indeed, shallow mesoscale convective cells seem to occur mostly over oceans (Atkinson and

Zhang [1996]). Another reason could be the choice of data windows and filtering. The spectral analysis in the Minnesota experiment provided spectra with frequencies from 2×10^{-4} Hz from run durations of 75 min, while the Kansas data provided spectra at frequencies from 10^{-3} Hz, with run durations of 60 min. The two sets of spectra were both corrected for effects of filtering, for details see Kaimal et al. ([1976]) and Larsen ([1986]).

Some may also argue that over the sea, during convective conditions, the underlying ocean swell may affect the air–sea momentum exchange and accordingly the atmospheric turbulence structure, e.g. Nilsson et al. ([2012]) and Wu et al. ([2018]). Such a contribution from swell is most effective at very small wind speeds of a few m s^{-1}. During our case, the mean wind speed is high, being about 16 m s^{-1}. The wave measurements from the FINO 1 site in the North Sea show the largest wave age (wave phase velocity at peak frequency divided by wind speed at 10 m) during the period of our case to be about 1, suggesting that the sea is young and our case is not complicated with the effect of swell.

Due to the difficulties in using the conventional parameter L and z_i, we therefore propose to include the stability effect through a mesoscale spectral model and use the boundary-layer turbulence model for neutral conditions only (e.g. through the Kaimal or the Mikkelsen model). The final model, expressed as in Eq. 8 or Eq. 10, is a simple superposition of a mesoscale spectrum and a microscale spectrum. Together with measurements, it is shown that the calculation of σ_U, one key parameter in wind energy, is significantly improved by introducing the mesoscale spectral model.

6 Conclusion

We examined the wind spectrum in the presence of open cells over the ocean using measurements from two sites about 100 km apart. We conclude that in the presence of open cells:

– The spectral gap is ill-defined and the significant spectral energy is associated with open cells.
– Existing boundary-layer models for the unstable wind spectrum involving z_i/L cannot be straightforwardly extended to include mesoscale aspects of open-cell convection. The stability is argued to be of large scale and can be included in the mesoscale model, $Aa_1 f^{-5/3}$, which is calibrated through standard 10-min data (from measurements or numerical modeling), with A obtained through regression.
– Existing boundary-layer turbulence models underestimate the low-frequency variation of wind speed, but new models that combine mesoscale variability and boundary-layer turbulence models significantly improve the calculation of the wind-speed variance. It is especially so for the enhanced mesoscale variability in the presence of open-cell structures, as reported here.

References

Atkinson BW, Zhang JW (1996) Mesoscale shallow convection in the atmosphere. Rev Geophys 4:403–431

Bakan S, Schwarz E (1992) Cellular convection over the north-eastern atlantic. Int J Climatol 12:353–367

Brummer B, Rump B, Kruspe G (1992) A cold air outbreak near spitsbergen in spring time: boundary layer modification and cloud development. Boundary-Layer Meteorol 61:13–46

Busack B, Bakan S, Luthardt H (1985) Surface conditions during mesoscale cellular convection. Bull Am Meteorol Soc 54:4–10

Businger JA, Wyngaard JC, Izumi Y, Bradley E (1971) Flux-profile relationships in the atmospheric surface layer. J Atmos Sci 28:181–189

Cheynet E, Jakobseb JB, Reuder J (2018) Velocity spectra and coherence estimates in the marine atmospheric boundary layer. Boundary-Layer Meteorol 169:429. https://doi.org/10.1007/s10546-018-0382-2

Courtney M, Troen I (1990) Wind speed spectrum for one year of continuous 8 hz measurements. In: Nineth symposium on turbulence and diffusion, American Metrorol Society, pp 301–304

Etling D, Brown RA (1993) Roll vortices in the planetary boundary layer: a review. Boundary-Layer Meteorol 65:215–248

Floors R, Lea G, Peña A, Karagali I, Ahsbahs T (2016) Report on RUNE's coastal experiment and first inter-comparisons between measurements systems. Wind Energy Department, Roskilde. Tech Rep DTU Wind Energy-E-Report-0115 (EN). http://orbit.dtu.dk/files/127277148/final.pdf

Gage K, Nastrom G (1985) On the spectrum of atmospheric velocity fluctuations seen by MST/ST radar and their interpretation. Radio Sci 20:1339–1347

Gage K, Nastrom G (1986) Theoretical interpretation of atmospheric wavenumber spectra of wind and temperature observed by commercial aircraft during GASP. J Atmos Sci 43:729–740

Heggem T, Lende R, Løvseth J (1998) Analysis of long time series of coastal wind. J Atmos Sci 55:2907–2917

Högström U, Hunt J, Smedman AS (2002) Theory and measurements for turbulence spectra and variances in the atmospheric neutral surface layer. Boundary-Layer Meteorol 103:101–124

Højstrup J (1982) Velocity spectra in the unstable boundary layer. J Atmos Sci 39:2239–2248

Kaimal J, Finnigan J (1994) Atmospheric boundary layer flows. Oxford University Press, New York, p 289

Kaimal J, Wyngaard J, Izumi Y, Coté O (1972) Spectral characteristics of surface-layer turbulence. Q J R Meteorol Soc 98:563–589

Kaimal J, Wyngaard J, Haugen J, Coté O, Izumi Y, Caughey S, Readings CJ (1976) Turbulence structure in the convective boundary layer. J Atmos Sci 33:2152–2169

Kim K, Adrian R (1999) Very large-scale motion in the outer layer. Phys Fluids 11:417–422

Larsen SE (1986) Hotwire measurements of atmospheric turbulence near the ground. Tech Rep Risø-R-233, Risø National Laboratory, Roskilde. ISBN 87-550-0056-8

Larsen SE, Højstrup J, Olsen H (1985) Parameterization of the low frequency part of spectra of horizontal velocity component in the stable surface boundary layer. In: Proceeings of the models of turbulence and diffusion in stably stratified regions of the natural environment. Clarendon Press, pp 181–204

Larsén XG, Vincent CL, Larsen SE (2013) Spectral structure of the mesoscale winds over the water. Q J R Meteorol Soc 139:685–700. https://doi.org/10.1002/qj.2003

Larsén XG, Larsen SE, Petersen EL (2016) Full-scale spectrum of boundary-layer winds. Boundary-Layer Meteorol 159:349–371

Larsén XG, Bolaños R, Du J, Kelly M, Koefoed-Hansen H, Larsen S, Karagali I, Badger M, Hahmann A, Imberger M, Sørensen JT, Jackson S, Volker P, Petersen O, Jenkins A, Graham A (2017a) Final report for X-WiWa project: extreme winds and waves for offshore turbines. Report DTU Wind Energy E-0154. ISBN: 978-87-93549-22-7. http://orbit.dtu.dk/files/139272513/FinalReport_PSO12020_XWiWa_20171031.pdf or Final Project Report on http://www.xwiwa.dk/main-results

Larsén XG, Du J, Bolaños R, Larsen SE (2017b) On the impact of wind on the development of wave field during storm Britta. Ocean Dyn 67(11):1407–1427. https://doi.org/10.1007/s10236-017-1100-1

Larsén XG, Petersen EL, Larsen SE (2018) Variation of boundary-layer wind spectra with height. Q J R Meteorol Soc. 1–13 https://doi.org/10.1002/qj.3301

LeMone M (1976) Modulation of turbulence energy by longitudinal rolls in an unstable planetary boundary layer. J Atmos Sci 33:1308–1320

Lilly D, Petersen E (1983) Aircraft measurements of atmospheric kinetic energy spectra. Tellus 35A:379–382

Lindborg E (1999) Can the atmospheric kinetic energy spectrum be explained by two-dimensional turbulence? J Fluid Mech 388:259–288

Mann J (1994) The spatial structure of neutral atmospheric surface-layer turbulence. J Fluid Mech 273:141–168

Mehrens AR, Hahmann AN, Larsén XG, von Bremen L (2016) Correlation and coherence of mesoscale wind speeds over the sea. Q J R Meteorol Soc 142:3186–3194

Mikkelsen T, Larsen SE, Jørgensen HE, Astrup P, Larsén XG (2017) Scaling of turbulence spectra measured in strong shear flow near the earth surface. Phys Scr 92(124):002

Nilsson E, Rutgersson A, Smedman AS, Sullivan P (2012) Convective boundary-layer structure in the presence of wind-following swell. Q J R Meteorol Soc 138:1476–1489. https://doi.org/10.1002/qj.1898

Peña A, Floors R, Wagner R, Courtney M, Gryning SE, Salthe A, Larsén XG, Hahmann AN, Hasager C (2016) Ten years of boundary-layer and wind-power meteorology at Høvsøre, Denmark. Boundary-Layer Meteorol 158:1–26

Petersen EL (1975) On the kinetic energy spectrum of the atmospheric motions in the planetary boundary layer. Tech Rep RISØ285, Risø National Laboratory, Roskilde. http://www.risoe.dk/rispubl/reports_INIS/RISO285.pdf

Smedman AS (1991) Occurrence of roll circulation in a shallow boundary layer. Boundary-Layer Meteorol 51:343–358

Smedman AS, Bergström H, Högström U (1995) Spectra, variance and length scales in a marine stable boundary layer dominated by a low level jet. Boundary-Layer Meteorol 76:211–232

Smedman-Högström AS, Högström U (1974) Spectral gap in surface-layer measurements. J Atmos Sci 32:660–672

Sørensen P, Hansen A, Rosas P (2002) Wind models for simulation of power fluctuations from wind farms. J Wind Eng Ind Aerodyn 90:1381–1402

Sørensen P, Cutululis NA, Vigueras-Rodríguez A, Madsen H, Pinson P, Jensen LE, Hjerrild J, Donovan M (2008) Modelling of power fluctuations from large offshore wind farms. Wind Energy 11:29–43

Tchen C, Larsen S, Pécseli H, Mikkelsen T (1985) Large-scale spectral structure with a gap in the stably stratified atmosphere. Phys Scr 31:616–620

Van der Hoven I (1957) Power spectrum of horizontal wind speed in the frequency range from 0.0007 to 900 cycles per hour. J Meteorol 14:160–164

Vincent CL (2010) Mesoscale wind fluctuations over danish waters. Risø-PhD; No 70(EN), PhD thesis. ISBN 978-87-550-3864-6

Vincent CL, Larsén XG, Larsen SE, Sørensen P (2013) Cross-spectra over the sea from observations and mesoscale modelling. Boundary-Layer Meteorol 146:297–318

Vinnichenko NK (1970) The kinetic energy spectrum in the free atmosphere—1 second to 5 years. Tellus 22:158–166

Wu L, Hristov T, Rutgersson A (2018) Vertical profiles of wave-coherent momentum flux and velocity variances in the marine atmospheric boundary layer. J Phys Ocean. https://doi.org/10.1175/JPO-D-17-0052.1